Pertanika J. Sci. & Technol. 34 (S2): 165 - 192 (2026)

PERTANIKA JOURNALS

SCIENCE & TECHNOLOGY

Journal homepage: http://www.pertanika.upm.edu.my/

An Optimised Deep Learning Framework for Skin Lesion Classification Using ResNet150 and M-GSO

Gurram Sunitha[1]*, Ahmed Elngar[2], Pravin R. Kshirsagar[3], and Subba Rao Polamuri[4]

[1]Department of Computer Science and Engineering, School of Computing, Mohan Babu University, Sree Sainath Nagar, Tirupati 517102, Andhra Pradesh, India
[2]Faculty of Computers and Artificial Intelligence, Beni-Suef University, Beni-Suef 62511, Egypt
[3]Department of Electronics and Telecommunication Engineering, J D College of Engineering and Management, Borgaon Fata, Kalmeshwar Road, Nagpur 441501, Maharashtra, India
[4]Department of Computer Science and Engineering, School of Computing, Aditya University, Aditya Nagar, ADB Road, Surampalem 533437, Kakinada District, Andhra Pradesh, India

ABSTRACT

Skin cancer is among the most prevalent cancers worldwide, affecting approximately 10 million people, and early diagnosis is critical for effective treatment. Manual assessment of dermoscopic images is time-consuming and prone to inter-clinician inconsistency, motivating the need for reliable automated classification systems. While deep networks offer strong representation power, training very deep models often faces challenges such as vanishing gradients, poor convergence, and overfitting. This paper proposes a modified ResNet150 architecture combined with a Leaky ReLU with Adaptive Factor (LRAF) activation to improve convergence and information flow across layers. To further enhance training, a Modified Group Search Optimisation (M-GSO) algorithm is employed for hyperparameter tuning, balancing exploration and exploitation in the search space. Experiments were conducted on the ISIC 2018 dataset, with data augmentation and SMOTE applied to address class imbalance. The proposed ResNet150 with M-GSO framework outperformed baseline ResNet150 and its non-optimised variants, achieving 98% sensitivity, 98.5% precision, 99% AUC, and high training stability. An ablation study confirmed that M-GSO optimisation plays a critical role in boosting accuracy and reducing false positives, while cross-dataset evaluation on ISIC 2019 and HAM10000, without retraining, demonstrated stable generalisation. These results indicate a trade-off between accuracy and computational cost, as M-GSO improves performance at the expense of increased tuning time. Overall, the findings show that integrating deep residual learning with adaptive activations

ARTICLE INFO

Article history:
Received: 03 August 2026
Accepted: 23 October 2026
Published: 20 November 2026

DOI: https://doi.org/10.47836/pjst.34.S3.08

E-mail addresses:
gurramsunitha@gmail.com (Gurram Sunitha)
elngar_7@yahoo.co.uk (Ahmed Elngar)
pravinrk88@yahoo.com (Pravin R. Kshirsagar)
psr.subbu546@gmail.com (Subba Rao Polamuri)
* Corresponding author

e-ISSN: 2231-8526

© Universiti Putra Malaysia Press

and population-based optimisation yields a more accurate and reliable solution for automated skin lesion classification.

Keywords: Group search optimiser, hyperparameter optimisation, medical image analysis, ResNet150, skin lesion classification

INTRODUCTION

Access to reliable medical services is essential for the public to lead a healthy life. People living in rural and urban regions lack access to medical services due to shortages of medical professionals and equipment. So, it becomes tough for patients to access standard and better medical services (Zhang et al., 2021). The healthcare industry can overcome this inaccessibility by employing modern technologies in two probable approaches. The first step is to use the Internet of Things (IoT) to shift medical care beyond hospitals and connect various medical devices. As a second step, the quality of healthcare services can be enhanced using modern Deep Learning (DL) methodologies (Li et al., 2021). In the last ten years, the dangerous form of skin cancer known as malignant Melanoma has increased dramatically. It is triggered by abnormal skin cell growth. Melanomas are otherwise called malignant lesions; they begin at the melanocyte level and spread in the skin's upper regions. The parts exposed to direct sunlight are highly prone to this disease. When malignant melanoma is not detected in the early stages, it will lead to a high death rate (Naqvi et al., 2023). The World Health Organisation (WHO) states that every year, 3 million or more cases of non-melanoma and 132,000 cases of melanoma are identified globally (World Health Organisation, 2017). The World Health Organisation reports 9,500 cases of skin cancer every day. The statistics indicate that there has been a 47% growth in invasive melanoma cases in the past decade. In 2022, 331,772 skin cancer cases were diagnosed worldwide, with nearly 66,000 cases of mortality (Ferlay et al., 2024). The number of males diagnosed with skin cancer is nearly 174,000, and the number of females diagnosed with skin cancer is nearly 151,000. The mortality cases were 32,000 and 25,000, respectively (International Agency for Research on Cancer, 2022).

By 2042, the expected number of new cases of Melanoma is 106,110, and the estimated number of deaths is 7,180 (Ferlay et al., 2024). The statistics above show an increase in melanoma cases. When overall cancer cases are considered, 75% of skin cancer deaths are due to Melanoma. The number of new melanoma cases discovered each year in Australia is 15,628. In Europe, the number of new cases reported yearly exceeds 20,800. Furthermore, an average of 1200 to 20,000 deaths occurs every year in Australia and Europe due to Melanoma. Since the 1990s, the skin cancer detection rate has increased steadily. The rise in skin cancer cases is mainly linked to ozone layer depletion and greater use of solariums, which expose people to harmful ultraviolet radiation. Prolonged exposure to

such radiation increases the risk of abnormal skin cell growth, leading to higher chances of cancer development. However, a recent statistic reveals that the survival rate can be increased up to 98% if skin cancer symptoms are spotted in their early stages.

Skin lesions may show variations in colour (brown, black, red, pink) and irregular shapes. Such heterogeneity, particularly the presence of multiple colours, is often associated with malignant lesions and may indicate disease progression or severity. To identify possible melanoma, naevi with abnormal colour and a diameter of 6 mm or more are more likely to be associated with the disease. Since lesions can vary in texture and colour, the primary identification of skin cancer is a challenging task (Dildar et al., 2021). Firstly, a dermatologist visually examines factors such as shape, size, lesion diameter, and abnormalities in mole colour. Then dermatologists use the following primary methods for diagnosing skin lesions. The pattern evaluation checklist using 7 points and the ABCD rule (edge, diameter, asymmetry, and colour) is used, along with dermoscopy and biopsy. In recent years, dermatologists have used microscopic and dermoscopy imaging techniques for skin cancer diagnosis (Esteva et al., 2017). A mobile camera can view the microscopic images as low-resolution images are produced. Dermoscopy is a method used by dermatologists to visually examine and diagnose malignant skin cancer lesions.

However, the above mentioned approaches face several challenges due to the following reasons: (i) dermoscopic and skin lesion images are often low-contrast making precise detection of lesions hard, (ii) diseased and healthy areas often share similar colors, making classification difficult and thereby increasing misclassification rate, (iii) lesions occurring on image boundaries lead to segmentation errors, (iv) segmentation accuracy is affected by variations in brightness of the image, (v) complex nature of lesions having various types, sizes, colours, textures and shapes (vi) few lesions are erroneously segmented due to appearance of hair, bubbles and blood vessels, (vii) visual variation among the intra and inter type skin lesions, and (viii) slight resemblance among the lesions types which makes the classification process more complex (Goyal et al., 2020). Unbalanced datasets are also a big issue for classification. Since classes with many images dominate those with fewer, there will be a considerable difference in classifier performance. Additionally, other possible difficulties with these methodologies are the use of handcrafted approaches, which leads to (a) the model's overfitting problem and (b) the high computational cost. The issues mentioned above can be minimised using the proposed ResNet150-M-GSO model for early detection of skin cancer. The work proposes its significant contributions as follows:

- In the preprocessing step, resizing, correlation, and normalisation improve the visibility of image edge details. Data augmentation is applied to increase dataset diversity and balance classes, helping the model generalise better.
- A depth-extended ResNet architecture (ResNet150) is constructed to enhance hierarchical feature representation for dermoscopic texture analysis.

- Feature extraction is enhanced using a Modified Group Search Optimisation (M-GSO) strategy, improving prediction performance through effective hyperparameter optimisation.
- The 150-layer deep network performs feature fusion, where only the most significant features are selected to achieve optimal outcomes.
- A fully connected network-based classifier is used for final feature classification. This ensures reliable lesion detection.
- The proposed model's stability is verified through a comprehensive statistical analysis, and the results are compared with those of recent methodologies.
- Dermatologists can save a considerable amount of time in identifying skin cancer and, at the same time, provide improved recognition accuracy. The proposed method achieves superior results with low computational time.

RELATED WORKS

High-resolution lesion images reduce skin reflectivity, allowing dermatologists to examine deeper skin structures. However, other skin cancer types and melanoma have similar features, which makes cancer diagnosis more difficult for even experienced dermatologists. Hence, a thorough and careful lesion diagnosis is crucial. This difficulty delays dermatologists' diagnosis of melanoma, thereby reducing the patient's chance of survival. So, diagnosing the disease at an early stage is vital, sparing the patient the painful biopsy process and improving the patient's chances of survival (Giuffrida et al., 2020).

Meanwhile, the process of skin lesion recognition done manually, even by experienced dermatologists through dermoscopy, consumes too much time, along with a high error rate and only 75% accuracy is achieved for melanoma detection. Researchers focus more on techniques such as automated detection systems to address Melanoma and its diagnostic challenges. Therefore, several Computer-aided diagnosis (CAD) methods have been proposed by researchers to address concerns regarding lesion detection, such as reduced detection time, and to simplify this diagnostic procedure by using DL methods to recognise skin lesions efficiently and automatically in the early phase from dermoscopic images (Iqbal et al., 2023). Modern skin lesion detection techniques make the diagnostic tool even more capable of classifying Melanoma and non-melanoma skin lesions (Bikku et al., 2018).

An improved VGG model is developed to enhance the accuracy of skin cancer detection (Tabrizchi et al., 2023). The study demonstrated performance gains by refining network depth and feature extraction. A skin cancer detection method using VGG16 and VGG19 with transfer learning is proposed (Faghihi et al., 2024). The results showed high accuracy, demonstrating the effectiveness of deep feature extraction from pretrained networks. Their study highlights transfer learning as a strong approach for medical image classification.

To enable dermatologists to identify skin lesions accurately and quickly, CAD approaches are used extensively in clinical imaging (Taye, 2023). Dermatologists depend on CAD methods for a second opinion. For skin lesion detection, the building blocks in CAD systems are image acquisition, feature extraction, segmentation, selection of skin image datasets and their fusion, and classification of skin lesion types. Deep features are extracted from deep neural layers (Bikku & Satya Sree, 2020). They are then utilised for classification. Deep feature analysis encompasses the image's local and global information, whereas traditional methodologies use features such as the skin lesion's shape, texture, and colour. The convolutional layers give global and local information (Asadi et al., 2023). During the segmentation phase, the wound area and boundaries of the infected region are often thin and difficult to delineate. In the classification phase, these localised lesions must be accurately assigned to their respective classes, such as benign keratosis, nevus, or melanoma (Raval & Undavia, 2023).

Various methodologies have been proposed to address segmentation and classification challenges, but none has consistently achieved high accuracy (Morid et al., 2021). Skin cancer has multiple categories, yet clinically, melanoma and benign lesions are most relevant. Differentiating melanoma from benign lesions enables high binary classification accuracy (Hasan et al., 2021). Some approaches follow a sequential process for initial lesion segmentation, identifying regions of interest and extracting discriminative features. These are then fed to a classifier model for final lesion categorisation. Classification accuracy largely depends on the quality of feature extraction (Bikku, 2020). Most studies treat feature selection and classification as separate processes; however, evaluating features experimentally is often more effective, as some important features may otherwise be overlooked. Accurate classification requires precise identification of local lesion regions to improve overall performance (Gajera et al., 2023).

Skin lesions are classified using binary classification. Extending this to multi-class classification is more challenging because many lesions share similar characteristics (Asif et al., 2025). Many classification methods rely only on deep learning–based feature extraction (Alwakid et al., 2022). However, redundant features are often not addressed, leading to errors in multi-class lesion classification. So, selecting the most suitable features and fusing them for final classification is crucial (Ji et al., 2024). Recently, accuracy has been significantly enhanced by selecting optimal features and fusion methods (A et al., 2024). The literature describes various selection and fusion methods. Improving the object information from different sources is the central goal of the fusion approach.

RESEARCH METHODOLOGY

This section provides a detailed discussion of the ResNet150 with the M-GSO framework to attain accurate skin cancer classification. This approach integrates an optimiser and deep models to improve the classification performance.

Data Preprocessing

The preliminary step in every image-based analysis is image preprocessing, in which raw images and their quality are enhanced to make the input more suitable for analysis (Altamimi et al., 2024). For skin cancer image classification, the following processes are included in the pre-processing step: resizing and cropping, rescaling, normalisation, colour correction, and noise reduction.

Data Augmentation

Data augmentation is employed to artificially increase diversity of the training data (Kebaili et al., 2023). Various transformations are applied to input images to improve the learning model's generalisation. This process aims to improve the learning model's robustness and performance. The data augmentation step involves deliberately modifying images during the training process. The data augmentation step is performed with careful consideration of numerous transformation techniques. Table 1 summarises the data augmentation performed on the training dataset. These operations are chosen based on the efficiency of dataset diversification. It is intended to handle image classification problems by exposing the model to different data variations.

Table 1
Data augmentation parameters used to enhance the diversity of the training dataset

Process	Range
Rescaling	1/255
Rotation	±20%
Width/Height Shifting	±20%
Zooming	±30%
Horizontal Flipping	Enabled

The proposed work employed data augmentation to attain triple advantage. First, the training dataset's size is significantly expanded, which is valuable when working with limited data resources. Second, the system can generalise and perform effectively in unexposed scenarios since the model is trained on diverse data variations. Third, data augmentation addresses certain issues, such as eliminating overfitting by introducing noise into the dataset. The learning model's reliability, performance and generalisation capabilities are significantly improved by data augmentation.

Leaky ReLU Activation Function (LRAF)

The commonly employed activation function is ReLU. The statistical expression in Equation 1 represents the ReLU function.

$$ReLU = \begin{cases} 0 & w < 0 \\ w & w \geq 0 \end{cases} \quad [1]$$

However, in this research, LRAF is proposed instead of the ReLU function. The problem of dead neurons in the ReLU function is eliminated by employing LRAF (Dubey

& Jain, 2019; Mastromichalakis, 2020). A slight negative slope for every negative input value introduced by the dead ReLU is handled by LRAF. It deals with the even gradient flow for negative inputs. The LRAF activation function is mathematically expressed as in Equation 2.

$$f(w) = \begin{cases} w & w \geq 0 \\ bw & w < 0 \end{cases} \quad [2]$$

While training the model, the factor 'b' is produced unevenly and it will turn into a static value. This procedure permits one-sided limitation by preserving specific harmful gradient data, thereby eliminating the overall loss. LRAF is utilised to concatenate and reshape every layer. When enormous noise is present, generating a non-zero output value is required to identify a negative input value; thereby, data leakage is avoided. The system's performance can be enhanced by minimising image noise. The advantages of ResNet and LRAF in this research are aimed at improving image classification. Owing to LRAF's specific advantages, it is combined with the ResNet model to provide faster execution and computation. ResNet is used alongside LARF to enhance the deep network's training performance and convergence while preventing gradient vanishing. Figure 1 presents the comparison of ResNet block structures using ReLU activation and LRAF activation.

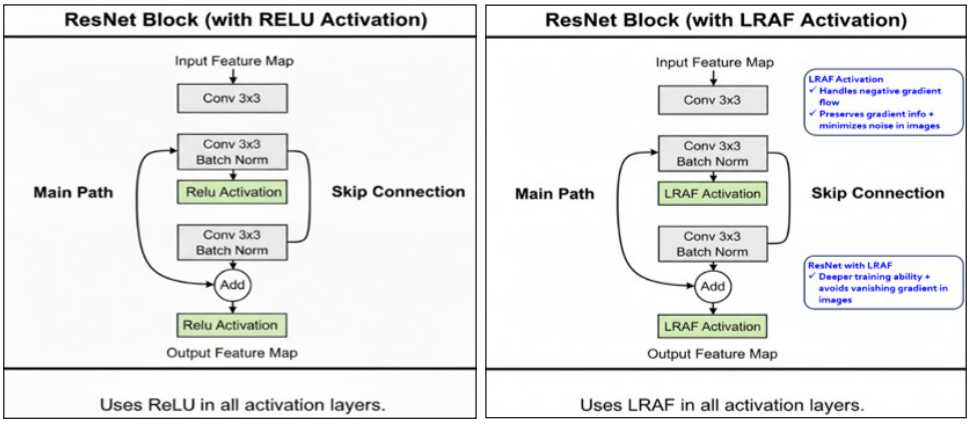


Figure 1. Comparison of ResNet block structures using ReLU activation (left) and LRAF activation (right)

ResNet150 Deep Model

Figure 2 presents the layer architecture of the proposed ResNet150. The proposed ResNet150 comprises 150 layers. ResNet-50 is extended by adding additional convolutional blocks, resulting in a deeper architecture referred to as ResNet150.

- conv3_x stage: 8 blocks (vs 4 in ResNet-50)
- conv4_x stage: 36 blocks (vs 6 in ResNet-50)

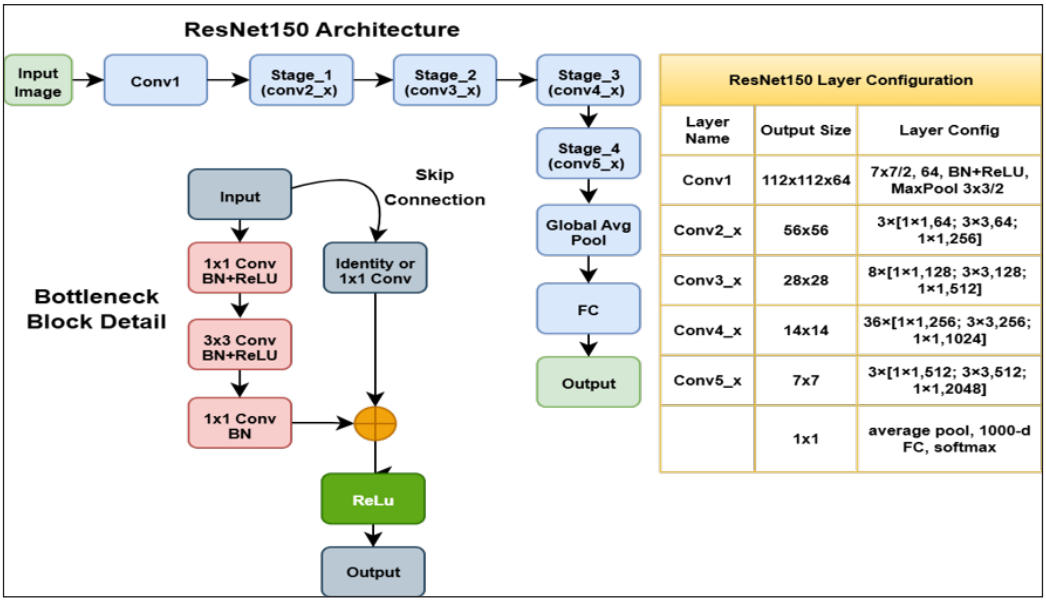


Figure 2. Architecture of ResNet150, illustrating convolutional stages, bottleneck blocks, and layer configuration for classification

ResNet150 (Residual Neural Network) includes 150 deep layers. The ResNet model comprises multiple stages, each containing identity and convolutional blocks. The pre-processed image is fed to the ResNet model based on Equation 3 given below:

$$J(y) = M(y) + y \quad [3]$$

In Equation 3, the input image is denoted by y The non-linear layer mapping is represented as $M(y)$ and the residual mapping is denoted as $J(y)$.

The convergence is more challenging in deep networks. LRAF is employed to avoid loss of input information. LRAF includes an alpha parameter, resulting in a minor but nonzero slope. Previously inactive nodes in ReLU will now alter their weights. A modified ResNet model for skin cancer classification substitutes the standard ReLU activations with LRAF activations. So, LRAF and ResNet150 are combined to enhance ResNet150's training ability, performance, and convergence. Thereby eliminating the vanishing gradient problem. The above change is done throughout the network, i.e., in fully connected layers and residual blocks. As an alternative to ReLU, the output of every convolutional layer in ResNet150 is passed to the residual block using the LRAF activation function. The LRAF with a convolutional layer is expressed as Equation 4 given below:

$$O_c = L_R\left(B_N(C_{2D}(I, F, K_s))\right) \quad [4]$$

Here, the convolutional layer output is denoted as O_c, LRAF is represented as L_R, and batch normalisation is represented as B_N. 2D convolution operation is denoted as C_{2D}. I denote input, F denotes filters, and Ks denotes kernel size. The Conv2D's output is normalised using batch normalisation. The embedded LRAF in the residual block is given by Equation 5 below.

$$O_R = L_R\ (B_N(C_{2D}(I), C_{2D}(I))) \quad [5]$$

Optimisation

The Modified-GSO (M-GSO) is proposed to optimise the hyperparameters of ResNet150, as it provides a better balance between exploration and exploitation than PSO, GA, and Bayesian optimisation. Other models often suffer from local optima/slower convergence. In preliminary trials, M-GSO achieved faster convergence and more stable performance on medical image classification tasks. Unlike SGO, M-GSO is implemented by improving the global search phases. The greedy selection technique is used in each phase to select a new population stronger than the previously chosen one. The linear population reduction approach in the exploration system supports exploration and allows transition from exploration to exploitation.

Global Search

The quality of the solution is improved by exploring the leader. A self-introspection factor acts as a control mechanism by imposing a restriction on the population velocity. This is followed by a greedy selection phase, in which fit members are retained, and non-fit members are discarded. This procedure works quite well for both multimodal and unimodal problems. But it often fails in dynamic search by being overly dependent on its leaders, resulting in very low efficiency when shifting composite functions. If a member's condition does not improve under this greedy selection mechanism, the population will stall, allowing lower-fitness solutions to be eliminated.

This enhanced phase explores a broader search space while simultaneously learning from the leader's experience. This phase is divided into two stages: the improved explorative phase, which is responsible for function evaluation, and the exploitative phase, as defined in Equation 6.

The following equations describe the position update mechanism of M-GSO. Each candidate solution is influenced by three main forces:

i. attraction towards the leader to find the best solution

ii. repulsion from the worst solution to avoid poor regions

iii. stochastic differential perturbations between randomly selected population members to maintain diversity.

These components collectively balance global exploration and local exploitation during optimisation.

$$\vec{P}_{new}\ (t+1) = \begin{cases} NFE < 0.5 * total\ NFE, Explorative \\ else, Exploitative \end{cases} \quad [6]$$

A large population is available at the beginning of the search process, which is used to promote the enhanced exploration phase. New solutions are generated by employing diverse vectors over the current population to explore the search space. The new solution is obtained from Equations 7-14. Choose a member P_r randomly from the population pool. Equation 7 updates the position of candidate solution $P_{i,j}$ at iteration t+1. An update occurs if the fitness of the current solution i is better than that of the reference solution r. R controls the influence of i. r1, r2, r3 are random coefficients for exploration. X1, Y1, Z1 represent search directions. Equation 8 represents the direction from i to r. It encourages movement toward a neighbour solution. Equation 9 represents the direction from r towards the leader solution. It guides search towards the current best candidate (leader). Equation (10) calculates the difference between the reference and worst solutions. It helps avoid poor search areas. Equation 11 is an alternative update rule that uses the control parameter CDC_DCD. It influences movement toward good solutions while reducing the influence of poor ones. Equation 12 directs i towards the leader. It creates a strong pull towards the best solution. Equation 13 directs r2 towards the leader. It maintains population diversity by incorporating an additional peer reference. Equation 14 calculates the contrast between another candidate and the worst solution. It balances exploration by avoiding worst-performing regions.

$$If\ f(P_i) < f(P_r).\ P_{i,j}^{(t+1)} = R * \vec{P}_{i,j}^{(t)} + r1 * \left[\vec{X}_1\right] + r_2 * \left[\vec{Y}_1\right] + r_3 * [\overrightarrow{Z_1}] \quad [7]$$

$$\vec{X}_1 = [\vec{P}_{r,j}^{(t)} - P_{i,j}^{(t)}] \quad [8]$$

$$\vec{Y}_1 = [Leader_j - P_{r,j}^{(t)}] \quad [9]$$

$$\vec{Z}_1 = [\vec{P}_{r,j}^{(t)} - \overrightarrow{worst_t}] \quad [10]$$

$$P_{i,j}^{(t+1)} = C_D * P_{r,j}^{(t)} - r_1 * \left[\vec{X}_2\right] - r_2 * \left[\vec{Y}_2\right] - 0.1 * [\vec{Z}_2] \quad [11]$$

$$\vec{X}_2 = [Leader_j - P_{i,j}^{(t)}] \quad [12]$$

$$\vec{Y}_1 = [Leader_j - P_{r2,j}^{(t)}] \quad [13]$$

$$\vec{Z}_1 = [\vec{P}_{2,j}^{(t)} - \overrightarrow{worst}_t] \quad [14]$$

Equations 7 to 14 together control directional movement toward promising regions while preventing premature convergence. The difference vectors increase population diversity, whereas leader-guided movement accelerates convergence toward optimal hyperparameter combinations.

To enhance the diversity of the population, difference vectors $\vec{X}$, $\vec{Y}$, and $\vec{Z}$ are introduced. $\vec{P}_{i,j}^{(t)}$ indicates the location of i^{th} population for j^{th} dimension in t^{th} iteration. $\vec{P}_{r,j}^{(t)}$ and $\vec{P}_{r2,j}^{(t)}$ signify any two randomly selected population members' positions from the present iteration. A random number denoted as *R*, takes values from 0 to 1. It is updated dynamically in each iteration. The finest solution gained so far is $Leader_j$ and the least good solution from the present iteration obtained is $\overrightarrow{worst}_t$. The success history is the dynamic self-introspection factor in the range [0.1, 1]. The reason for including the worst solution is to allow and preserve increased diversity during the exploration process. At any given point, multiple difference vectors help avoid solution clustering, and adaptive self-introspection enables the particle to explore and navigate the solution space in a controlled manner. The exploitation phase of M-GSO performs actual position updates. It includes a new system for feedback position updates with a probabilistic selection between the two approaches, as expressed in Equations 15 to 19. Equation 15 represents the exploitation phase (move towards the leader). sel > 0.5 is a probabilistic condition controlling exploitation. CR is a control parameter that regulates the step size. $P_{i,j}^{(t)}$ is the current position of agent i in dimension j. $Leader_j$ is the position of the leader in dimension j. r1 is a random weight (0–1) adding stochasticity. Equation 15 pulls the solution closer to the leader, encouraging exploitation.

Equation 16 represents the exploration + diversification phase (influence of FB-leader, random peer, and FB-worst). F, whose value is $1+r+C_R$, introduces adaptive scaling. $P_{FB-leader,j}^{(t)}$ is the feedback-based leader position (best after reduction). $P_{r2,j}^{(t)}$ is the random peer solution. $P_{FB-worst,j}^{(t)}$ is the feedback-based worst solution. A correction factor of −0.01 helps avoid clustering near the worst solutions. This equation balances exploration (the difference between the leader and a randomly chosen peer) and diversification (moving away from the worst).

Equations 17 and 18 represent the dynamic handling of the best and worst solutions when the population size decreases. Equation 17 avoids this by dynamically selecting a

feedback-based leader in response to population updates. It maintains elitism by retaining the best solutions as N_P is reduced. Equation 18 is the rule for selecting the worst solution. Equation 19 represents adaptive scaling for stability. It is a scaling factor that adjusts search dynamics. rand adds randomness. C_R provides adaptive control. F allows for a balance between intensification (leader attraction) and diversification (avoiding the worst regions).

$$If\ sel > 0.5\ \ P_{i,j}^{(\vec{t}+1)} = C_R * \overrightarrow{P_{i,j}^{(t)}} + r_1 * [leader_j = P_{i,j}^{(\vec{t})} \quad [15]$$

$$Else\ \ P_{i,j}^{(\vec{t}+1)} = C_R * \overrightarrow{P_{i,j}^{(t)}} + F * \left[P_{FB-leade\,r_j}^{(t)} - P_{r2,j}^{(\vec{t})}\right] - 0.01 * [P_{r2,j}^{(\vec{t})} - P_{FB-wors\,t_j}^{(t)}] \quad [16]$$

$$P_{FB-leade\,r,j}^{(t)} = \begin{cases} FB - Leader, j & if\ N_P\ is\ reduced \\ P_{r,j}^{t} & else \end{cases} \quad [17]$$

$$P_{FB-worst\,,j}^{(t)} = \begin{cases} FB - worst, j & if\ N_P\ is\ reduced \\ P_{r,j}^{t} & else \end{cases} \quad [18]$$

$$F = 1 + rand + C_R \quad [19]$$

The exploitation scheme selector is represented as Sel. FB-Worst and FB-Leader denote the worst and best solutions in the rejected population. They supply feedback to the present population.

Observing Phase

The M-GSO observing phase aims to enhance population diversity by leveraging comparative learning among the leader and population members. This phase builds on the idea of data exchange in a society where every member of the population communicates randomly with other members of the society and with the leader. Based on the two interacting members' intellects, information is gained or passed among the members of the population. Quick convergence is achieved during the observation phase, and population diversity decreases due to the addition of a greedy operator to each solution obtained. To enhance the production of a diverse population between the two population members, a fitness-based selection system is implemented by the adaptive observing phase. By employing this method, premature convergence caused by stagnation and entrapment can be avoided. With the current greedy selection technique, reinitialisation is not an option

since it contributes negligible diversity to the overall population. The population updates are given in Equation 20.

$$If\ f(P_i) < f(P_r)\ \ P_{i,j}^{(\vec{t}+1)} = P_{i,j}^{(\vec{t})} + C_D * [Leader_j - P_{r,j}^{(\vec{t})}]$$
$$else\ P_{i,j}^{(\vec{t}+1)} = P_{i,j}^{(\vec{t})} - C_D * [Leader_j - P_{r,j}^{(\vec{t})}] \quad [20]$$

Parameter Selection

The M-GSO performance can be improved by dynamically adapting the self-introspection factor to the sequence of failures and successes. Analysis of various inertial control settings shows that a static setting of c=0.2 yields good performance on both multi-modal and uni-modal landscapes. In contrast, inertia increases towards ccc as iterations progress, depending on the learning mechanism. The CD value is also adaptively adjusted to strengthen the exploration process, as shown in Equation 21.

$$CD_{new} = \begin{cases} CD_{old} & Failures < learning\ rate \\ \left(0.2 * C_{D_{int}}\right) + (0.2 * rand) & Failures \geq learning\ rate \end{cases} \quad [21]$$

In the adaptive technique, the CD value is retained for new population members that achieve improved fitness. When extreme failure counts occur, it is re-initialised. At initialisation, the failure value is set to zero. During the adaptive acquiring and enhanced improving phases, the failure counter is incremented by one for each unsuccessful member that does not generate better offspring. An empirical learning rate of 10 is used to ensure sufficient trials to form a fresh CD combination, thereby enhancing solution quality. The CR value is set within the range of 0.2 to 1.0, consistent with the standard SGO recommendations for c. At the end of each iteration, the CD value is updated, R is randomised between 0.1 and 1.0, and CD alterations are applied to avoid reliance on static control parameter settings. The failure counter update is represented in Equation 2, where f(x) is the fitness function value, xnew is the offspring, and xparent is the parent solution. At initialisation, Failure=0.

$$For\ each\ iteration, Failure = \begin{cases} 0, if\ f(x_{new}) < f(x_{parent}) \\ Failure + 1, Otherwise \end{cases} \quad [22]$$

Adaptive CD update is represented in Equation 23 where CDt is current CD value in iteration t, n is empirical learning rate (=10), F_{max} is threshold for maximum allowed failures, CD_{init} is reinitialised CD value.

$$If\ Failure < F_{max}\ then\ CD_{t+1} = CD_t + n\,.rand(0,1)$$
$$else\ CD_{t+1} = CD_{init} \quad [23]$$

CR adaptation is represented in Equation 24, where U denotes a uniform random distribution.

$$CR \in [0.2,1.0]\ ,R \sim U[0.1,1.0] \quad [24]$$

Exploration and Exploitation

In M-GSO, achieving an appropriate balance between exploration and exploitation is critical to improving convergence and avoiding premature stagnation. The algorithm integrates adaptive control strategies through Controlled Degree CD, Crossover Rate CR, and the self-introspection factor c to manage proper balance dynamically.

Exploration Phase

- Higher diversity is maintained during early iterations by adapting CD values dynamically. When a solution repeatedly fails, its CD is reinitialised, forcing it to search new areas. This prevents population stagnation and ensures that the algorithm explores across multiple dimensions of the search space.
- The CR parameter is randomised between 0.2 and 1.0, thereby enhancing solution variability and avoiding premature convergence.
- c adjusts the population's velocity.

Exploitation Phase

- Greedy selection ensures that only solutions with improved fitness are retained, intensifying the search around promising regions.
- The adaptive learning mechanism modifies CD based on successful offspring, ensuring local refinement while discarding redundant or unfit members.
- The revised differential mutation operator further improves local search by fine-tuning around high-quality candidates.

Dynamic Balance

- The adaptive exploration–exploitation balance enables M-GSO to discover optimal regions globally and refine solutions locally, outperforming static search strategies. In the initial iterations, exploration of the global space is achieved using high CD values

and a randomised CR value. Over iterations, exploitation takes over, implemented using optimised CD values.

Complexity Analysis

M-GSO algorithm updates population positions once in each phase- the improving phase and the acquiring phase. Each update is followed by greedy selection, which ensures inferior solutions are discarded, and better ones are retained. At each iteration, this process yields two fitness evaluations per population member. The total computational complexity of M-GSO is determined by initialisation, fitness evaluations, position updates, and greedy selection. Let P_S be the population size, and PD be the problem dimension. Initialisation requires O ($P_S \times P_D$). Fitness evaluations, including the population, improvement, and search phases, each require O (PS × PD) time. The observing and selection phases require O(P_S) per iteration. For T iterations, the overall computational complexity O (T × PS × PD) is dominated by fitness evaluations and position updates. Since each fitness evaluation is performed twice in each iteration, the total number of function evaluations is 2×PS×T. The total computational time of the M-GSO is represented in Equation 25.

$$t_{total} = t_1 + O_1 + t_2 * O_2 + \cdots + t_N * O_{Ps} \quad [25]$$

where $O_1, O_2, \ldots, O_{Ps}$ denote computational complexities of different operations performed in M-GSO for a population size of Ps. $t_1, t_2, \ldots, t_N$ are the amounts of computational time required for each operation. The algorithm in Figure 3 presents the detailed steps of the M-GSO algorithm.

Table 2 summarises time requirements and complexities for the main phases of M-GSO. To provide a practical understanding of computational cost, consider PS = 50 (population size), PD = 5 (number of optimised hyperparameters), and T = 100 (iterations). The total number of fitness evaluations is 2 × PS × T = 2 × 50 × 100 = 10,000.

Table 2
Computational time intervals of different phases and time complexity in the proposed algorithm

Functionality	Time Interval	Complexity of Sub-Operation	Complexity of M-GSO
Initialise	t_1	O($P_S \times P_D$)	
Fitness based on population	t_2	O($P_S \times P_D$)	
Fitness based on improvement	t_3	O($P_S \times P_D$)	O($T \times P_S \times P_D$)
Fitness on searching	t_4	O($P_S \times P_D$)	
Observing phase	t_5	O(P_S)	
Selection phase	t_6	O(P_S)	

```
Start
Initialize the input parameters
Set learning rate and failure rate
Generate initial population randomly based on dimensional size
Predict worst and gbest
for t = 1 to T do
    for I = 1 to Np do
        Role assignment:
            Select one head searcher (guides direction)
            Select side searchers (explore nearby space)
            Select rear searchers (exploit around current best)
        Improvement phase:
            Head updates position using global direction
            Side searchers update positions at ±90° to head
            Rear searchers move toward historical gbest
        Compute new candidate positions P_new(t+1)
        Update failure rate and learning rate adaptively
    End for
    Update worst solution and gbest;
    Acquiring phase:
        Select random agent r, set i ≠ r
        if f(P_i) < F(P_r) then:
            Accept new candidate P_i^{i,j}(t+1)
        else
            Retain current candidate P_i^{i,j}(t)
        Update gbest after acquisition
        Verify termination condition
    End for
    Stop
```

Figure 3. M-GSO algorithm

Modified GSO swaps GSO's vision-based producer/scrounger/ranger movement for three fixed-geometry roles (head/side/rear) and adds memory via rear searchers moving toward historical gbest. It introduces adaptive learning and failure rates to self-tune step sizes, which standard GSO lacks. It adds a separate "Acquiring Phase" with greedy pairwise tournament selection (accept only if better than a randomly selected peer) — a mechanism borrowed from algorithms such as TLBO/ABC, not part of traditional GSO.

RESULTS AND DISCUSSIONS

Skin lesion images for model training were obtained from the ISIC Challenge 2018 dataset. It contains 1197 malignant and 1440 benign samples (Codella et al., 2019). The dataset

is partitioned using stratified random sampling into training (75%) and testing (25%) subsets, preserving the original class distribution. The test set comprises 660 images (300 malignant and 360 benign). No preprocessing, augmentation, or optimisation procedures were performed on the test dataset.

As the dataset exhibited class imbalance, oversampling was applied only to the training data to balance the classes. SMOTE technique was used, followed by data augmentation techniques including rotation, horizontal flipping, scaling, brightness jitter, and noise injection. Then, the training dataset is expanded to 2,000 images per class (malignant and benign). This procedure ensured that the testing dataset remained independent. Thereby preventing data leakage and guaranteeing unbiased performance evaluation. Figure 4 presents sample input and pre-processed images from the training set.

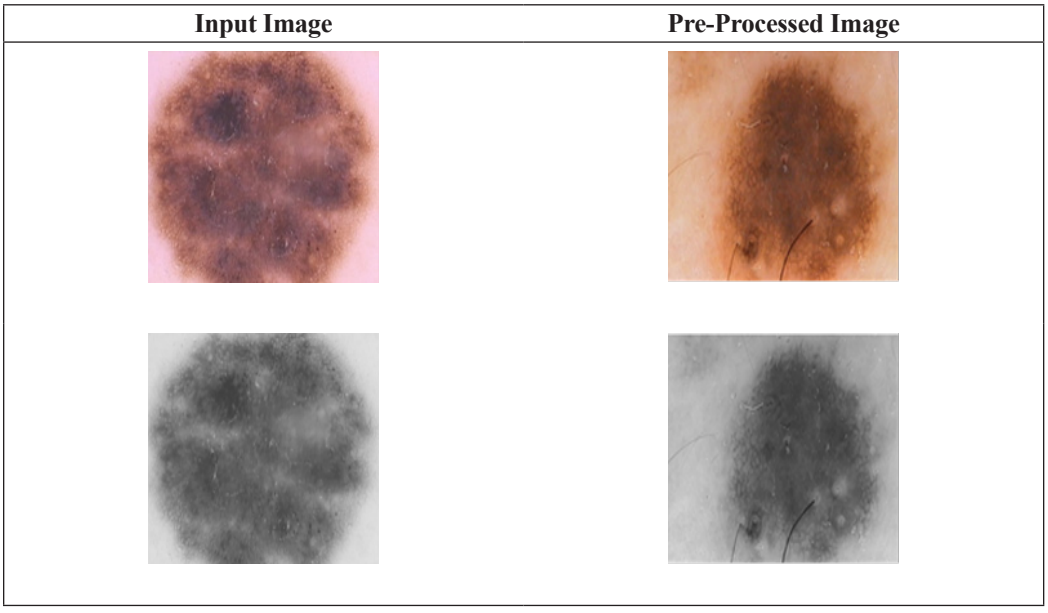


Figure 4. Results of the pre-processing stage showing enhanced and normalised input images

In ResNet150 with M-GSO, the training batch size is fixed at 32, and the number of epochs is set to 25. The model achieved stable accuracy improvements with this setup. During training, dropout rates of 0.2 and 0.4 were applied to reduce overfitting. These dropout values helped balance the trade-off between model generalisation and accuracy. The validation accuracy is consistent with the training accuracy, indicating better generalisation by the algorithm.

Further experiments were performed by changing the learning rate while keeping the batch size fixed. It is observed that a learning rate of 0.001 provided the best accuracy, reaching 97%. When the learning rate was increased, the model suffered from unstable

convergence, while a lower rate slowed training. Based on these observations, the learning rate of 0.001 is finalised for the next training runs.

Different image sizes were tested to analyse their effect on accuracy. With the training batch fixed at 32 and the learning rate at 0.001, image sizes of 128, 160, and 224 were used. The results showed that 224 × 224 provided the highest accuracy, while smaller sizes reduced training time but slightly lowered precision. Hence, 224 × 224 is selected for subsequent experiments.

Table 3 presents the initial hyperparameter search space explored by M-GSO during optimisation. These values define the candidate ranges evaluated by the optimiser. The final selected configuration after optimisation is reported separately in Section 4.1.

Table 3
Hyperparameter search space explored by M-GSO

Component	Parameter	Value / Setting
M-GSO	Population size	50
	Number of iterations	100
	CDCD initialisation	Random within [0,1]
	Factor / Step size	0.5
	Patience	1
ResNet150 Backbone	Number of layers	150
	Training batch size	32 – 64
	Learning rate	0.0001 – 0.001
	Dropout rates	0.2 – 0.5

Figure 5 presents the experimental results of ResNet150 with the M-GSO learning model. The proposed model's performance during training is assessed using various performance metrics. The M-GSO is used as a hyperparameter optimisation technique to select suitable values for hyperparameters such as learning rate, batch size, and dropout rate. Once these hyperparameters are chosen, the Adam optimiser is used during training to update the model weights. Adam optimiser is used with a learning rate of 0.001, and categorical cross-entropy is the loss function used. ReduceLROnPlateau callback is used with a factor of 0.5 and patience of 1. Then, ResNet150 with the M-GSO model is trained using both the validation and training datasets.

Different combinations of dropout rates within the defined search range (0.2–0.5) were evaluated through the M-GSO optimisation process. It was observed that using a lower dropout rate in the first layer and a moderately higher rate in deeper layers effectively controlled overfitting. When the dropout rate exceeded 0.5, model accuracy decreased significantly due to underfitting. The final selected dropout values were 0.2 and 0.4. They provided the best balance between training stability and generalisation performance.

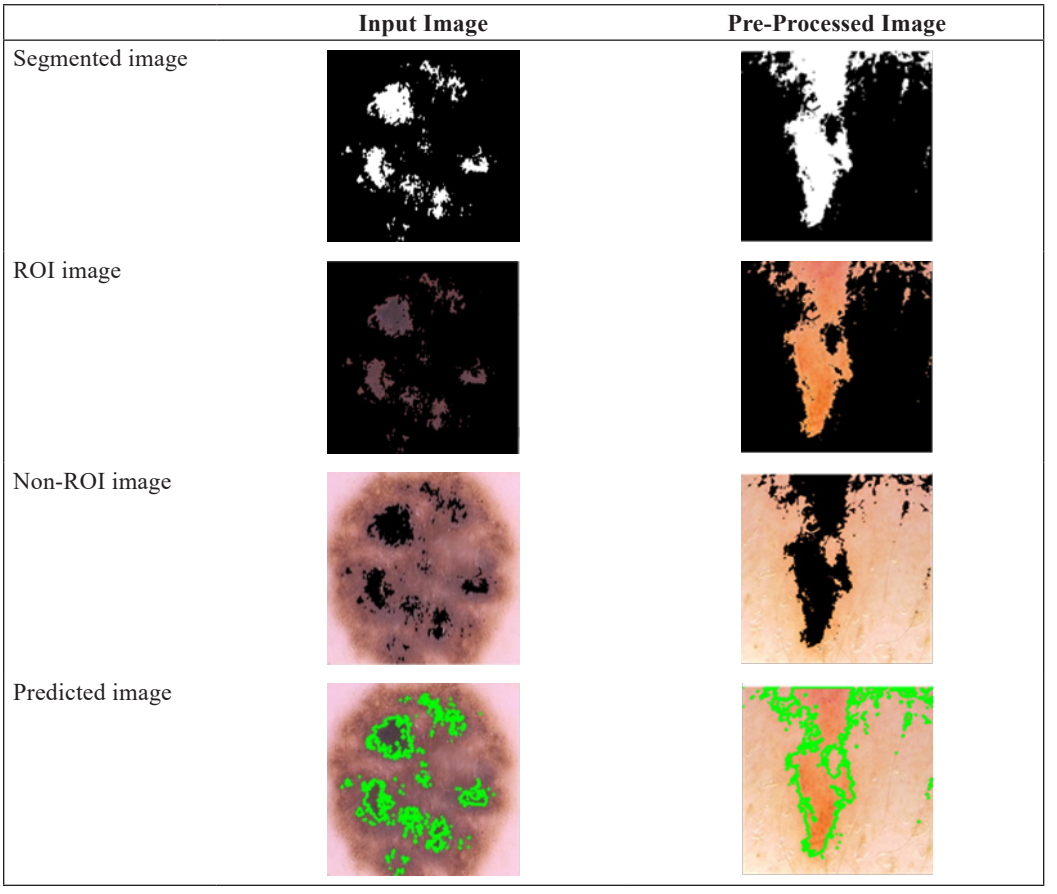


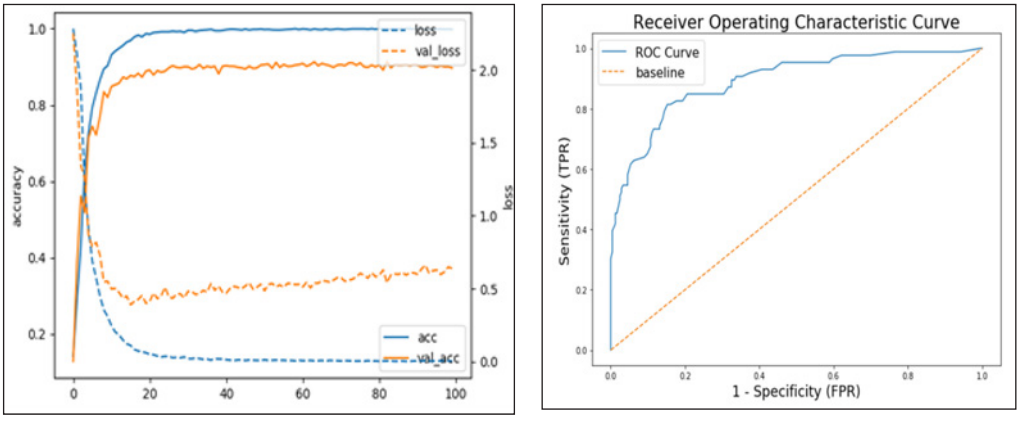
Figure 5. Predicted images highlighting classification results of ResNet150 with M-GSO

Based on the M-GSO optimisation process within the defined search space, the final adopted training configuration is as follows: learning rate = 0.001, batch size = 32, first-layer dropout rate = 0.2, second-layer dropout rate = 0.4, input image size = 224 × 224. All final performance results reported in this study are obtained using this optimised configuration. The effect of the number of epochs is also studied by training ResNet150 with M-GSO for 30, 50, and 100 epochs. The validation and training accuracies increased sharply during the first 10 epochs. After epoch 20, accuracy stabilised at 100% training and 96% validation. Beyond epoch 30, accuracy improvements were negligible, and the model converged.

The training loss decreased rapidly during the first 5 epochs, then gradually declined until epoch 20, where it stabilised. Validation loss followed a similar pattern, reaching stability around 0.12. After epoch 30, both training and validation losses remained consistent, indicating that the model had converged. The efficiency of ResNet150 with M-GSO is evaluated using ROC curves and AUCs across all classes. The model achieved an overall AUC of 99%, with the highest class-specific AUC of 98% and the lowest of

78%. These results confirm that Algorithm 1 achieves reliable classification performance, with stable accuracy and balanced generalisation (Figure 6).

The accuracy and loss curves in Figure 6(a) show that after a few epochs, training accuracy rises sharply and stabilises near 1.0. Validation accuracy also increases and stabilises near 0.9. Thus, showing strong generalisation. Training loss decreases quickly to almost zero. Validation loss stabilises around 0.4–0.5. This indicates that M-GSO-tuned ResNet150 is effective in fitting the data while avoiding severe overfitting. ROC curve in Figure 6(b) shows high sensitivity across different specificity values. The curve remains well above the baseline, with area close to 1.0. This reflects the strong discriminative ability of the proposed model.



(a) (b)

Figure 6. (a) Training and validation accuracy and loss curves across epochs; (b) roc curve showing classification sensitivity–specificity trade-off

A binary classification model, such as the skin cancer recognition model, can be evaluated using the AUC metric. A higher AUC indicates better model performance and discriminative power in distinguishing negative and positive samples. AUC scores expose relative performance and strengths of various DL models for skin cancer classification. When AUC scores are compared, the optimisation achieves superior performance. The ROC curve is generated for each category, and the corresponding AUC values are computed. The proposed model achieved an overall AUC of 0.99, indicating strong discriminative power. Category-specific AUC values ranged from 0.77 to 0.99, indicating that the proposed model is highly reliable across most categories, though certain categories exhibited moderate separability. These AUC values, combined with accuracy, precision, recall, and F1-score, validate the robustness of ResNet150 with M-GSO. Results confirm that ResNet150 combined with M-GSO achieves high accuracy, low error, and robust classification performance for skin lesions.

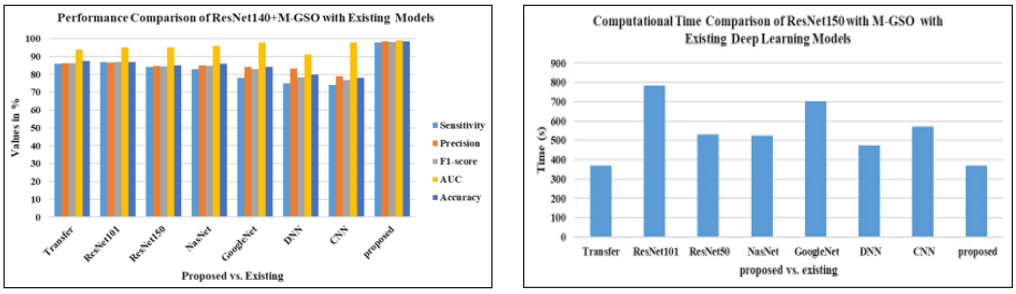
This research work demonstrates that the strengths of different DL models can be efficiently enhanced by integrating appropriate optimisers, thereby improving generalisation capabilities and accuracy for tasks such as skin cancer image classification.

Comparison with Benchmark Learning Models

Table 4 compares ResNet150 with M-GSO and existing approaches for skin lesion classification, including transfer learning with ResNet50, ResNet101, NASNet, GoogleNet, DNN, and CNN. The performance results of the existing approaches were obtained from their respective published studies and are presented as literature-based benchmark results for reference. These models were not retrained using the dataset split and experimental settings used for the proposed ResNet150 with M-GSO model. Here, various metrics such as sensitivity, precision, F1-score, FPR, AUC, accuracy, and time. The proposed model attained 98% sensitivity, whereas ResNet101, ResNet50, NASNet, GoogleNet, DNN and CNN approaches attained 86%, 87%, 84%, 83%, 78%, 75% and 74%, respectively. The precision of the proposed ResNet150 with M-GSO is 98.5%, whereas the other models attain 86.4%, 86.7%, 84.7%, 85.1%, 84%, 83.1% and 79%, respectively. The F1-score of ResNet150 with M-GSO is 98.1%, higher than that of other approaches. The existing models attain 86.3%, 87%, 84.5%, 84.6%, 83%, 78.4% and 76.8%.

Table 4
Performance comparison of ResNet150 with M-GSO with existing deep learning models

Classification Approaches	Sensitivity (%)	Precision (%)	F1-Score (%)	FPR	AUC	Accuracy (%)	Time (s)
Transfer learning with ResNet50 (Hossain et al., 2022)	86	86.4	86.3	0.02	94	87.6	368
ResNet101 (He et al., 2016)	87	86.7	87	0.02	95	87	784
ResNet50 (He et al., 2016)	84	84.7	84.5	0.03	95	85	532
NasNet (Zoph et al., 2018)	83	85.1	84.6	0.02	96	86	526
GoogleNet (Szegedy et al., 2015)	78	84	83	0.03	98	84	703
DNN (LeCun et al., 1998)	75	83.1	78.4	0.03	91	80	473
CNN (Hinton et al., 2012)	74	79	76.8	0.04	98	78	571
Proposed ResNet150 + M-GSO	98	98.5	98.1	0.01	99	98.5	350



(a) (b)

Figure 7. (a) Performance comparison of ResNet150 with M-GSO with existing deep learning models; (b) Computational time comparison of ResNet150 with M-GSO with existing deep learning models

The FPR of the proposed ResNet150 with M-GSO is 0.01, which is lower than that of existing approaches. The AUC of ResNet150 with M-GSO is 99%, approximately 1% to 8% higher than that of other approaches. The accuracy of the proposed ResNet150 with M-GSO is 98.5%, substantially higher than that of other approaches. The execution time of the proposed model is 350 s, which is less than that of the other approaches. Based on this analysis, the classification accuracy of the proposed model is higher than that of existing benchmark approaches such as transfer learning with ResNet50, ResNet101, NASNet, GoogleNet, DNN, and CNN (Figures 7a and 7b).

In the proposed setup, ResNet150 extracts deep image features, but its training requires fine-tuned hyperparameters. M-GSO improved this step by assigning search roles. The head searcher directed the exploration of new hyperparameter values globally. It avoided local minima by trying distant search positions. The side searchers explored variations around the head position. Their search at ±90° provided diversity and prevented convergence into narrow regions.

M-GSO tuned hyperparameters of ResNet150 for balanced exploration and exploitation. The integration allowed ResNet150 to focus on high-quality feature extraction while M-GSO ensured optimal training dynamics.

M-GSO improves hyperparameter tuning by exploring diverse solution spaces, but it incurs additional computational cost. This cost is higher than grid search or Bayesian optimisation because M-GSO maintains a population of candidate solutions. The overhead is controlled by limiting the search space and using early stopping inside each M-GSO cycle. Yet the method still requires more resources than lightweight optimisers. This forms a trade-off between performance and computational power. While the approach improves accuracy and stability, it may not suit low-resource or real-time clinical settings. Future work will focus on reducing the tuning cost through hybrid optimisation strategies.

The FPR of the proposed ResNet150 with M-GSO is 0.01, which is lower than that of existing approaches. The AUC of ResNet150 with M-GSO is 99%, approximately 1% to

8% higher than that of other approaches. The accuracy of the proposed ResNet150 with M-GSO is 98.5%, substantially higher than that of other approaches. The execution time of the proposed model is 350 s, which is less than that of the other approaches. Based on this analysis, the classification accuracy of the proposed model is higher than that of existing benchmark approaches such as transfer learning with ResNet50, ResNet101, NASNet, GoogleNet, DNN, and CNN (Figure 7).

In the proposed setup, ResNet150 extracts deep image features, but its training requires fine-tuned hyperparameters. M-GSO improved this step by assigning search roles. The head searcher directed the exploration of new hyperparameter values globally. It avoided local minima by trying distant search positions. The side searchers explored variations around the head position. Their search at ±90° provided diversity and prevented convergence into narrow regions.

Ablation Study

Table 5 and Figure 8 show a comparison between ResNet150 and M-GSO, with the optimisation approach removed, for skin lesion classification. The functionality of the proposed ResNet150 is analysed by eliminating M-GSO to evaluate various metrics. The proposed model gives 98% sensitivity, whereas ResNet150 without M-GSO attains 89%. The precision of the proposed ResNet150 without M-GSO is 86.5%, whereas the proposed model attains 98.5%. The F1-score of the proposed ResNet150 without M-GSO is 88.1%.

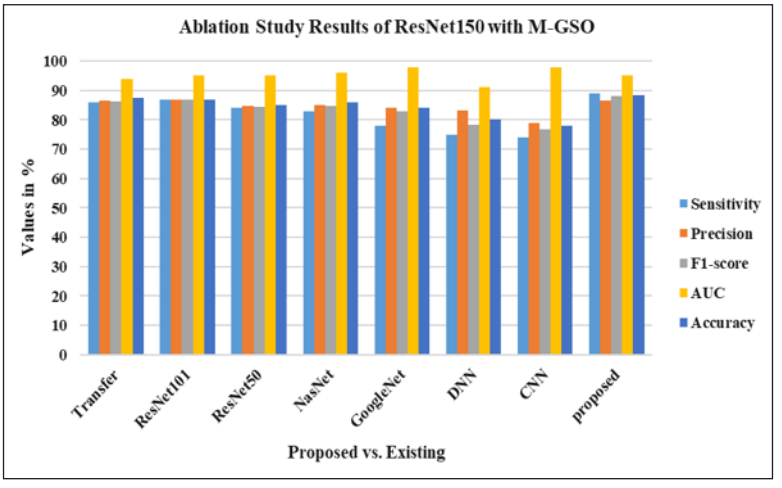


Figure 8. Ablation study results of ResNet150 with M-GSO

The FPR of the proposed ResNet150 without M-GSO is 0.04, which is comparatively higher than that of the proposed approach. The AUC of the proposed model is 99%, which is greater than that of ResNet150 without M-GSO. The accuracy of the proposed

Table 5
Ablation study results comparing performance metrics of model variants

Classification Approaches	Sensitivity (%)	Precision (%)	F1-score (%)	FPR	AUC	Accuracy (%)	Time (s)
Proposed ResNet150 with M-GSO	98	98.5	98.1	0.01	99	98.5	350
Proposed ResNet150 without M-GSO	89	86.5	88.1	0.04	95	88.5	370

Table 6.
Comparison of proposed model across ISIC 2018, ISIC 2019 (cross-dataset evaluation without retraining), and HAM10000 (cross-dataset evaluation without retraining)

Dataset	Sensitivity (%)	Precision (%)	F1-Score (%)	FPR	AUC	Accuracy (%)	Time (s)
ISIC 2018 (Trained + Tested)	98.0	98.5	98.1	0.010	99.0	98.5	350
ISIC 2019 (cross-dataset evaluation without retraining)	93.2	94.1	93.5	0.018	96.2	94.7	350
HAM10000 (cross-dataset evaluation without retraining)	91.5	92.3	91.8	0.021	95.5	92.8	350

ResNet150 without M-GSO is 88.5%. The time required to execute the proposed model is 350s. This ablation study highlights that network parameter optimisation is essential to enhance global prediction outcomes. M-GSO enables the model to achieve the global solution by addressing both exploration and exploitation strategies.

Cross-Dataset Evaluation Without Retraining

ISIC 2019 originally contains eight lesion categories. To maintain consistency with the binary classification model trained on the ISIC 2018 dataset, lesion labels were grouped into malignant and benign categories. Melanoma (MEL), basal cell carcinoma (BCC), and squamous cell carcinoma (SCC) were grouped as malignant, while nevus (NV), actinic keratosis (AK), benign keratosis (BKL), dermatofibroma (DF), and vascular lesions (VASC) were grouped as benign. The trained ISIC 2018 model was directly evaluated on this remapped binary version without retraining. Although HAM10000 exhibits a strong class imbalance in its original multi-class distribution, binary remapping reduces the severity of the imbalance. No rebalancing was applied during cross-dataset evaluation. Full k-fold cross-validation was not conducted due to computational limitations. However, consistent trends were observed across experimental runs.

Table 6 shows how the proposed model performs on ISIC 2018, ISIC 2019, and HAM10000 without retraining. The model reaches high sensitivity, precision, and AUC

on ISIC 2018, reflecting strong learning on the training dataset. When evaluated in cross-dataset evaluation without retraining on ISIC 2019 and HAM10000, the scores dropped slightly due to domain shift.

Performance drops on ISIC 2019 and HAM10000 are due to distribution shift. These datasets differ in image acquisition devices, lesion diversity, colour calibration, and annotation style. Hence, the datasets exhibited feature-level mismatch.

CONCLUSION

This work proposed a modified ResNet150 framework that integrates the LRAF activation and M-GSO optimisation for skin lesion classification. LRAF improved information flow and mitigated vanishing gradient issues, while M-GSO effectively tuned hyperparameters to achieve stable convergence and higher accuracy. On the ISIC 2018 dataset, the proposed model outperformed baseline ResNet150, achieving 98% sensitivity, 98.5% precision, and 99% AUC, with reduced false positives. An ablation study confirmed that the optimisation component significantly enhances network performance and robustness, and cross-dataset evaluation on ISIC 2019 and HAM10000, without retraining, demonstrated stable generalisation beyond the training distribution.

Despite these promising results, certain limitations remain. Training on high-resolution dermoscopic images demands considerable computational resources, which may constrain scalability for real-time clinical deployment. Additionally, although M-GSO improves hyperparameter tuning, it increases training time relative to standard approaches, reflecting a trade-off between accuracy and computational cost.

Future work will focus on four directions. First, evaluating the framework on larger, more diverse, multi-source datasets would further validate its generalisability. Second, incorporating lightweight network variants could improve inference speed and enable deployment on mobile or edge devices. Third, extending M-GSO to architecture search, rather than to hyperparameter tuning alone, may yield further performance gains. Finally, integrating clinical metadata with image-based features could support a more comprehensive decision-support system for early skin cancer diagnosis.

ACKNOWLEDGEMENT

I would like to express my sincere gratitude to my supervisor, Dr Ahmed Elngar, at the Faculty of Computers & Artificial Intelligence, Beni-Suef University, Beni Suef City, Egypt, for his valuable guidance and support during my Postdoctoral Fellowship. I am deeply thankful to my co-supervisors, Prof. Pravin R. Kshirsagar, J D College of Engineering & Management, Nagpur, India, and Dr Subba Rao Polamuri, Aditya University, Surampalem, India, for their valuable insights and continuous encouragement throughout my Postdoctoral Fellowship.

REFERENCES

A, R. S., Chamola, V., Hussain, Z., Albalwy, F., & Hussain, A. (2024). A novel end-to-end deep convolutional neural network based skin lesion classification framework. *Expert Systems with Applications, 246*, Article 123056. https://doi.org/10.1016/j.eswa.2023.123056

Altamimi, A., Alrowais, F., Karamti, H., Umer, M., Cascone, L., & Ashraf, I. (2024). An improved skin lesion detection solution using multi-step preprocessing features and NASNet transfer learning model. *Image and Vision Computing, 144*, Article 104969. https://doi.org/10.1016/j.imavis.2024.104969

Alwakid, G., Gouda, W., Humayun, M., & Sama, N. U. (2022). Melanoma detection using deep learning-based classifications. *Healthcare, 10*(12), Article 2481. https://doi.org/10.3390/healthcare10122481

Asadi, O., Yekkalam, A., & Manthouri, M. (2023). MDDC: Melanoma detection using discrete wavelet transform and convolutional neural network. *Journal of Ambient Intelligence and Humanized Computing, 14*(9), 12959-12966. https://doi.org/10.1007/s12652-022-04381-z

Asif, S., Qurrat-ul-Ain, Khan, S. U. R., Amjad, K., & Awais, M. (2025). SKINC-NET: An efficient lightweight deep learning model for multiclass skin lesion classification in dermoscopic images. *Multimedia Tools and Applications, 84*(13), 12531-12557. https://doi.org/10.1007/s11042-024-19489-x

Bikku, T. (2020). Multi-layered deep learning perceptron approach for health risk prediction. *Journal of Big Data, 7*(1), Article 50. https://doi.org/10.1186/s40537-020-00316-7

Bikku, T., Nandam, S. R., & Akepogu, A. R. (2018). A contemporary feature selection and classification framework for imbalanced biomedical datasets. *Egyptian Informatics Journal, 19*(3), 191-198. https://doi.org/10.1016/j.eij.2018.03.003

Bikku, T., & Satya Sree, K. P. N. V. (2020). Deep learning approaches for classifying data: A review. *Journal of Engineering Science and Technology, 15*(4), 2580-2594. https://jestec.taylors.edu.my/Vol%2015%20issue%204%20August%202020/15_4_32.pdf

Codella, N., Rotemberg, V., Tschandl, P., Celebi, M. E., Dusza, S., Gutman, D., Helba, B., Kalloo, A., Liopyris, K., Marchetti, M., Kittler, H., & Halpern, A. (2019). *Skin lesion analysis toward melanoma detection 2018: A challenge hosted by the International Skin Imaging Collaboration (ISIC)* [Preprint]. arXiv. https://doi.org/10.48550/arXiv.1902.03368

Dildar, M., Akram, S., Irfan, M., Khan, H. U., Ramzan, M., Mahmood, A. R., Alsaiari, S. A., Saeed, A. H. M., Alraddadi, M. O., & Mahnashi, M. H. (2021). Skin cancer detection: A review using deep learning techniques. *International Journal of Environmental Research and Public Health, 18*(10), Article 5479. https://doi.org/10.3390/ijerph18105479

Dubey, A. K., & Jain, V. (2019). Comparative study of convolution neural network's ReLU and leaky-ReLU activation functions. In S. Mishra, Y. R. Sood, & A. Tomar (Eds.), *Applications of computing, automation and wireless systems in electrical engineering: Proceedings of MARC 2018* (pp. 873-880). Springer. https://doi.org/10.1007/978-981-13-6772-4_76

Esteva, A., Kuprel, B., Novoa, R. A., Ko, J., Swetter, S. M., Blau, H. M., & Thrun, S. (2017). Dermatologist-level classification of skin cancer with deep neural networks. *Nature, 542*(7639), 115–118. https://doi.org/10.1038/nature21056

Faghihi, A., Fathollahi, M., & Rajabi, R. (2024). Diagnosis of skin cancer using VGG16 and VGG19 based transfer learning models. *Multimedia Tools and Applications, 83*(19), 57495–57510. https://doi.org/10.1007/s11042-023-17735-2

Ferlay, J., Ervik, M., Lam, F., Laversanne, M., Colombet, M., Mery, L., Piñeros, M., Znaor, A., Soerjomataram, I., & Bray, F. (2024). *Global Cancer Observatory: Cancer Today* (Version 1.1) [Data set]. International Agency for Research on Cancer. https://gco.iarc.who.int/today

Ferlay, J., Laversanne, M., Ervik, M., Lam, F., Colombet, M., Mery, L., Piñeros, M., Znaor, A., Soerjomataram, I., & Bray, F. (2024). *Global Cancer Observatory: Cancer Tomorrow* (Version 1.1) [Data set]. International Agency for Research on Cancer. https://gco.iarc.who.int/tomorrow

Gajera, H. K., Nayak, D. R., & Zaveri, M. A. (2023). A comprehensive analysis of dermoscopy images for melanoma detection via deep CNN features. *Biomedical Signal Processing and Control, 79*, Article 104186. https://doi.org/10.1016/j.bspc.2022.104186

Giuffrida, R., Conforti, C., Di Meo, N., Deinlein, T., Guida, S., & Zalaudek, I. (2020). Use of noninvasive imaging in the management of skin cancer. *Current Opinion in Oncology, 32*(2), 98-105. https://doi.org/10.1097/cco.0000000000000611

Goyal, M., Knackstedt, T., Yan, S., & Hassanpour, S. (2020). Artificial intelligence-based image classification methods for diagnosis of skin cancer: Challenges and opportunities. *Computers in Biology and Medicine, 127*, Article 104065. https://doi.org/10.1016/j.compbiomed.2020.104065

Hasan, M. R., Fatemi, M. I., Khan, M. M., Kaur, M., & Zaguia, A. (2021). Comparative analysis of skin cancer (benign vs. malignant) detection using convolutional neural networks. *Journal of Healthcare Engineering, 2021*, Article 5895156. https://doi.org/10.1155/2021/5895156

He, K., Zhang, X., Ren, S., & Sun, J. (2016). Deep residual learning for image recognition. In *2016 IEEE Conference on Computer Vision and Pattern Recognition (CVPR)* (pp. 770-778). IEEE. https://doi.org/10.1109/cvpr.2016.90

Hinton, G., Deng, L., Yu, D., Dahl, G. E., Mohamed, A.-R., Jaitly, N., Senior, A., Vanhoucke, V., Nguyen, P., Sainath, T. N., & Kingsbury, B. (2012). Deep neural networks for acoustic modeling in speech recognition: The shared views of four research groups. *IEEE Signal Processing Magazine, 29*(6), 82–97. https://doi.org/10.1109/msp.2012.2205597

Hossain, M. B., Iqbal, S. M. H. S., Islam, M. M., Akhtar, M. N., & Sarker, I. H. (2022). Transfer learning with fine-tuned deep CNN ResNet50 model for classifying COVID-19 from chest X-ray images. *Informatics in Medicine Unlocked, 30*, Article 100916. https://doi.org/10.1016/j.imu.2022.100916

International Agency for Research on Cancer. (2022, March 30). *Global burden of cutaneous melanoma in 2020 and projections to 2040* (Press Release No. 311) [Press release]. https://www.iarc.who.int/wp-content/uploads/2022/03/pr311_E.pdf

Iqbal, S., Qureshi, A. N., Li, J., & Mahmood, T. (2023). On the analyses of medical images using traditional machine learning techniques and convolutional neural networks. *Archives of Computational Methods in Engineering, 30*(5), 3173-3233. https://doi.org/10.1007/s11831-023-09899-9

Ji, Z., Wang, X., Liu, C., Wang, Z., Yuan, N., & Ganchev, I. (2024). EFAM-Net: A multi-class skin lesion classification model utilizing enhanced feature fusion and attention mechanisms. *IEEE Access, 12*, 143029-143041. https://doi.org/10.1109/access.2024.3468612

Kebaili, A., Lapuyade-Lahorgue, J., & Ruan, S. (2023). Deep learning approaches for data augmentation in medical imaging: A review. *Journal of Imaging, 9*(4), Article 81. https://doi.org/10.3390/jimaging9040081

LeCun, Y., Bottou, L., Bengio, Y., & Haffner, P. (1998). Gradient-based learning applied to document recognition. *Proceedings of the IEEE, 86*(11), 2278-2324. https://doi.org/10.1109/5.726791

Li, H., Pan, Y., Zhao, J., & Zhang, L. (2021). Skin disease diagnosis with deep learning: A review. *Neurocomputing, 464*, 364-393. https://doi.org/10.1016/j.neucom.2021.08.096

Mastromichalakis, S. (2020). *ALReLU: A different approach on Leaky ReLU activation function to improve neural networks performance* [Preprint]. arXiv. https://doi.org/10.48550/arXiv.2012.07564

Morid, M. A., Borjali, A., & Del Fiol, G. (2021). A scoping review of transfer learning research on medical image analysis using ImageNet. *Computers in Biology and Medicine, 128*, Article 104115. https://doi.org/10.1016/j.compbiomed.2020.104115

Naqvi, M., Gilani, S. Q., Syed, T., Marques, O., & Kim, H.-C. (2023). Skin cancer detection using deep learning—a review. *Diagnostics, 13*(11), Article 1911. https://doi.org/10.3390/diagnostics13111911

Raval, D., & Undavia, J. N. (2023). A comprehensive assessment of convolutional neural networks for skin and oral cancer detection using medical images. *Healthcare Analytics, 3*, Article 100199. https://doi.org/10.1016/j.health.2023.100199

Szegedy, C., Liu, W., Jia, Y., Sermanet, P., Reed, S., Anguelov, D., Erhan, D., Vanhoucke, V., & Rabinovich, A. (2015). Going deeper with convolutions. In *2015 IEEE Conference on Computer Vision and Pattern Recognition (CVPR)* (pp. 1-9). IEEE. https://doi.org/10.1109/cvpr.2015.7298594

Tabrizchi, H., Parvizpour, S., & Razmara, J. (2023). An improved VGG model for skin cancer detection. *Neural Processing Letters, 55*(4), 3715-3732. https://doi.org/10.1007/s11063-022-10927-1

Taye, M. M. (2023). Theoretical understanding of convolutional neural network: Concepts, architectures, applications, future directions. *Computation, 11*(3), Article 52. https://doi.org/10.3390/computation11030052

Zhang, B., Zhou, X., Luo, Y., Zhang, H., Yang, H., Ma, J., & Ma, L. (2021). Opportunities and challenges: Classification of skin disease based on deep learning. *Chinese Journal of Mechanical Engineering, 34*(1), Article 112. https://doi.org/10.1186/s10033-021-00629-5

Zoph, B., Vasudevan, V., Shlens, J., & Le, Q. V. (2018). Learning transferable architectures for scalable image recognition. In *2018 IEEE/CVF Conference on Computer Vision and Pattern Recognition* (pp. 8697-8710). IEEE. https://doi.org/10.1109/cvpr.2018.00907